Progress in the Development of Failure Maps : Negative Pressure-Strain-Temperature Diagram

Progress in the Development of Failure Maps ; Negative Pressure - Strain - Temperature Diagram*

Muneaki Shimura and Sakae Saito

The Research Institute for Iron, Steel and Other Metals

(Received July 31, 1980)

Synopsis

The paper describes the development of failure maps. These are maps with hydrostatic tensile stress as one axis and fracture strain as one axis and temperatures as the other, showing the fields of dominance of a given micromechanism of fracture : cleavage, ductile fracture, intergranular fracture, and so on.

Maps are presented for three structural steels, one high purity chromium stainless steel, one high strength aluminium alloy and one high strength titanium alloy. They give an overview of the micromechanisms by which a given material may fail, and help identify the one most likely to be dominant in a given experiment, or an engineering application. They should give guidance in selecting materials for low-temperature use and in selecting processing parameters in deformation processing of the materials.

I. Introduction

One of the essential features in understanding the mechanical behaviour of materials has been elucidation of the microstructual and atomistic factors which influence the competition between fracture and continued plastic flow in solids. Ductility in metalworking

---

* The 1716th report of the Research Institute for Iron, Steel and Other Metals.

applications, as expresses by some measure of deformation to fracture, is not a unique property of the material; it depends on localized conditions of stress, strain rate, and temperature in combination with material characteristics. The stress and strain state in a material during deformation processing is not uniform, but varies from point to point. Processing parameters determine these local stress and strain states throughout the material. Control of the parameters may thus be exercised to produce conditions favorable for enhanced deformations to fracture. For this purpose, a fracture criterion that predicts on combined stresses and/or strains at fracture in deformation processing would be useful. Several criteria of fracture are based on the well-known effect of hydrostatic pressure in suppression of ductile fracture and of tensile stresses in promoting fracture[1,2] , but the prediction of fracture through theoretical means alone is futile at the present stage of fracture-model development.[3]

Experimental determination of failure maps offers the best approach to workability problems at the present time. Ashby has recently expanded the utilization of such maps in stress-temperature space to demonstrate the relationships between failure modes at various strain rates[4,5]. The salient feature of his maps is to note that in general we must take cognizance not only of the competition between plasticity and fracture but also the competition between available fracture modes. This raises a third mode of utilization of failure map viz. the examination of the influence of stress state on the occurrence of a well defined and quantitatively characterized mode of failure[6]. To date little data is available on this aspect although some valuable progress has been made in the discussion of the influence of hydrostatic pressure on the strain to failure resulting from void nucleation and growth[2,7].

Furthermore, approximate hydrostatic tensile stress states are known to occur, for example, near the root of a notch and may contribute to the brittle fracture of nominally ductile materials. However, linear elastic fracture mechanics does not predict any influence of pressure on fracture toughness[8] although a back extrapolation might then show that the fracture toughness could decrease below the usual plane strain value[9].

This presentation illustrates the basic formalism for the portrayal of the failure behaviour of bulk materials under multiaxial stress state.

II. Failure Maps based on Direct Observation

This section describes failure maps for three structural steels, one stainless steel, one titanium alloy and one aluminium alloy. The axes of most of the maps are hydrostatic tensile stress component, fracture strain and temperature; a few are plotted using axes of stress and strain. They show the fields of dominance of each micromechanism of fracture: ductile fracture, intergranular fracture, cleavage fracture and so forth. The maps are based on our own experiments.

II. 1. Method of construction of the maps

The procedure is as follows. We first assemble the available tensile data under hydrostatic tensile stress state for the given material. The practical difficulties in testing to fracture under hydrostatic tension is well known. Previous attempts have included work on thermally induced stress fields, tests on notched tension specimen, tests on pocker-chip specimens and, most recently, tests on cubic or spherical specimens[10].

In his pioneering study on the effect of pressure on fracture, Bridgman obtained, for a given longitudinal profile radius of curvature on the neck of a round bar, an approximate solution for the distribution of stresses and plastic strain across the plane of the neck at the smallest cross section[11]. The stress distribution is shown in Fig. 1. Direct comparison of the extension of the Bridgman analysis for the distribution of negative pressure with the results of recent numerical computations[12] demonstrate that this solution is rather good near the neck, as shown in Fig. 2. Therefore, the necked region of a bar with its distribution of plastic strains and negative pressure along the axis is a convenient plastic flow field for experimental studies of fracture behaviour of materials[13]. Thus, Bridgman-type specimens were used in order to investigate the effect of hydrostatic tension on fracture behaviour of the materials.

In round bar with initially machined grooves, however, the axial plastic strain increments may no longer be uniform along the plane of the neck, as in predicted by the Bridgman solution, making that solution no longer valid[14]. The departure from a condition of uniaxial strain in bars with initially machined longitudinal profile is a result of a departure of the machined profile from the natural neck geometry[13]. So, in the first stage of the experiment, a number of

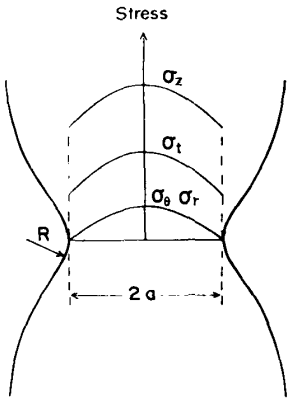

$$\sigma_z = Y[1+\ln(\frac{a^2+2aR-r^2}{2aR})]$$

$$\sigma_\theta = \sigma_r = Y\ln(\frac{a^2+2aR-r^2}{2aR})$$

$$\sigma_t = Y[\frac{1}{3}+\ln(\frac{a^2+2aR-r^2}{2aR})]$$

Fig.1 Stress distribution of the Bridgman-type specimen at the narrowest cross section.
σ_z: longitudinal stress componemt,
σ_θ: circumferential stress component,
σ_t: hydrostatic tensile stress compnent (negative pressure).
R is the minimum longitudinal (profile) radius of curvature at the neck, and a is the radius of the narrowest portion of the neck.

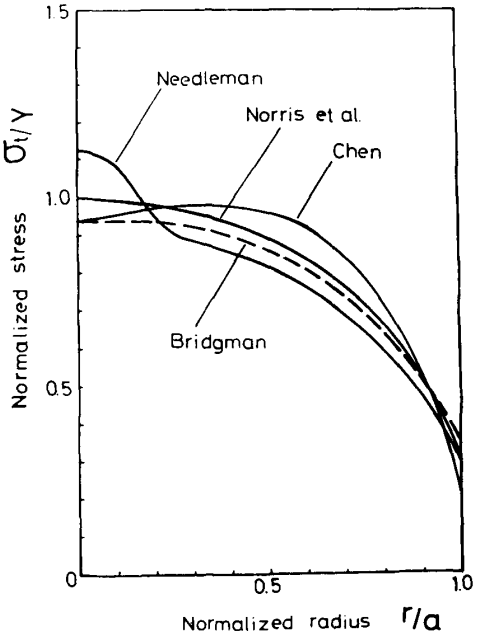

Fig.2 Comparison of negative pressure distribution obtained by Bridgman's analytical solution with the results of recent numerical computations.[12]

natural profiles of necks were carefully measured on a steel bar. From such measurements it was determined that the natural neck profile can be described with a high degree of accuracy by the empirical equation developed by Dondik[15], as follows.

$$r = r_m + A[e^{0.69(1-\frac{b}{x^2+b})} - 1]$$

where $A = r_u - r_m$; r_u, r_m is the radius of the specimen and minimum neck cross section, respectively, and b is the coefficient characterizing the properties of the material.

Bridgman-type specimens with a natural necking profile after Dondik equation were machined using a numerically controlled lathe, as shown in Fig. 3. The diameter of the narrowest portion of the neck of the specimen was 16 mm, and the minimum longitudinal radius of curvature at the neck was 3～45 mm. Figure 4 shows the results of the tension tests of a steel (S45C). The abscissa represents reduction of area, and the ordinate represents the value of maximum hydrostatic tensile component calculated from neck profile of the specimen. As seen in this figure, the value of maximum hydrostatic tensile component changes from initial value to final value in the deformation process.

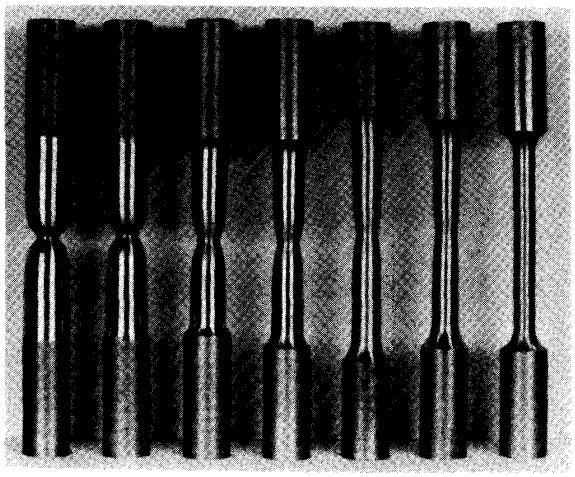

Fig.3 Bridgman-type specimens

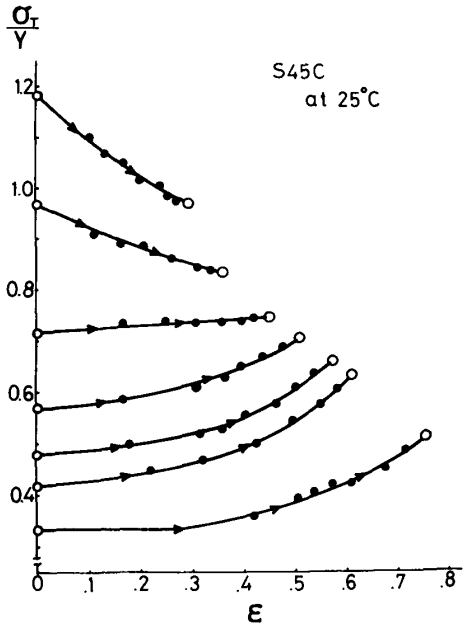

Fig.4 Variation of hydrostatic tensile component during tensile tests of the Bridgman-type specimens(S45C).

Second, we assign a mechanism of failure based on fractographic observations, though it can sometimes be inferred from sudden changes in ductility. For example, two types of transition from ductile to cleavage are involved in the process of fracture of the steel. The one is cleavage fracture as a function of negative pressure and the other is fibrous-cleavage transition in the growth of the crack. The fracture surface shows bimodal fracture in the range of transition pressure.

The information is then in the way shown in Fig. 5. The axes are fracture strain, ε_f , temperature, T , and mean maximum hydrostatic tensile stress component along deformation trajectory, normalized by flow stress, $(\bar{\sigma}/\sigma_Y)$; each datum is plotted as a symbol identifying the mode of failure. Open circles on Fig. 5 indicate that the fracture mechanism was overall fibrous fracture; double circles means bimodal (fibrous and cleavage) fracture; crossed circles denote overall cleavage fracture.

Third, fracture characteristics of material are expressed as a curved surface in three dimensional space (fracture strain - temperature - hydrostatic stress component) and boundaries shown by broken lines are drawn on the curved surface, separating blocks of data with a given mode of failure.

The method of constructing the map is illustrated for a steel (S45C) in Section II. 2. There are, of course, difficulties and ambiguities in a study of this sort. There are influences of many factors: strictly, a diagram applies to one composition of alloy, with one grain size and in one state of processing. Specimen size is important : rupture is favoured in slender bar, for instance, because the conditions are more nearly those of plane stress (where possible, we have selected data from round bar with dia. of 16 mm or greater). In spite of these difficulties,we have found the general form of the diagrams is reproducible.

II. 2. Commercial structural steels

II. 2. 1. The failure map for S 45 C (Fig. 5)

Figure 5, for S 45 C (commercial grade 0.45% Carbon, Table 1) is typical of failure maps for many structural steels.

Table 1 Chemical composition of S45C

(wt%)

C	Si	Mn	P	S	Cu	Ni	Cr
0.45	0.24	0.82	0.021	0.023	0.01	0.01	0.03

As seen in this diagram, the higher the hydrostatic tensile stress, the lower the fracture strain. It shows three mechanism fields between 25°C and -75°C. At high hydrostatic tensile stresses and at low temperatures, the steel fails by cleavage fracture. At low triaxiality and at high temperature, it fails by ductile fracture,

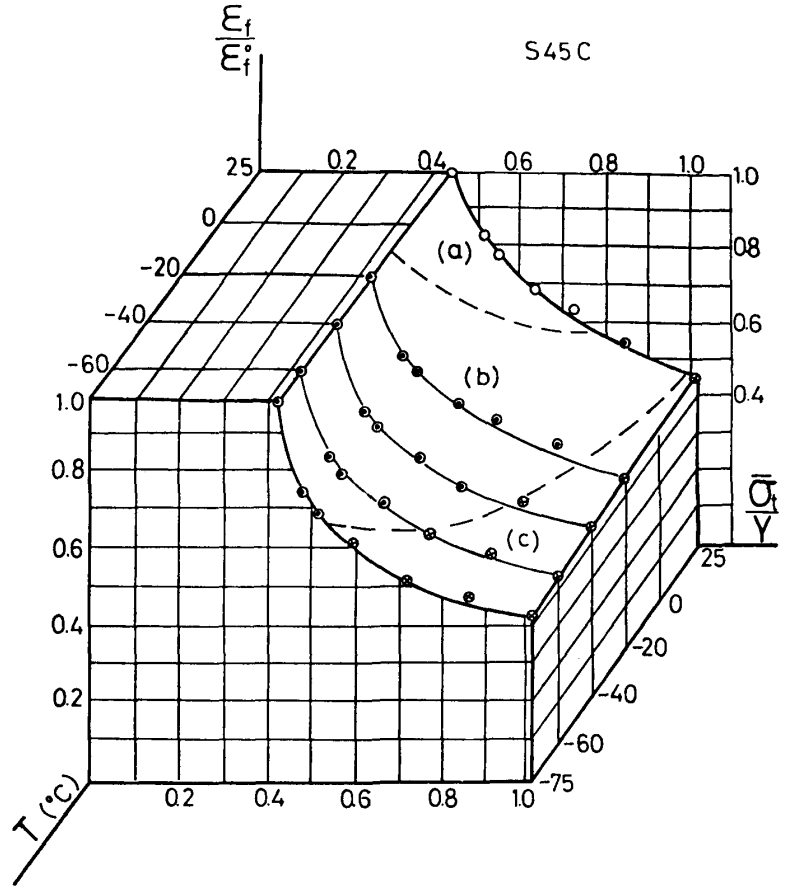

Fig.5 Failure map of S45C. $\varepsilon_f/\varepsilon_f^\circ$: fracture strain of the Bridgman-type specimens normalized by fracture strain of smoothed round bar specimen, T : temperature, σ/Y : mean maximum hydrostatic tensile stress normalized by flow stress. (cross-head speed : 0.5mm/min.)

that is by the formation of fibrous "cup", surrounded by a shear-lip or "cone", forming in the necked region of the specimen. As the temperature is decreased and the hydrostatic tensile stress is increased, it fails by bimodal fracture. In this range, fibrous fracture initiates in the central part of the neck and propagates radially and then a transition from fibrous to cleavage occurs during the propagation, as shown in Fig.6 and 7 . It is noticeable that two types of transition phenomena from ductile to cleavage are involved in the process of fracture. The one is as a function of negative pressure and the other is in the propagation of fracture.

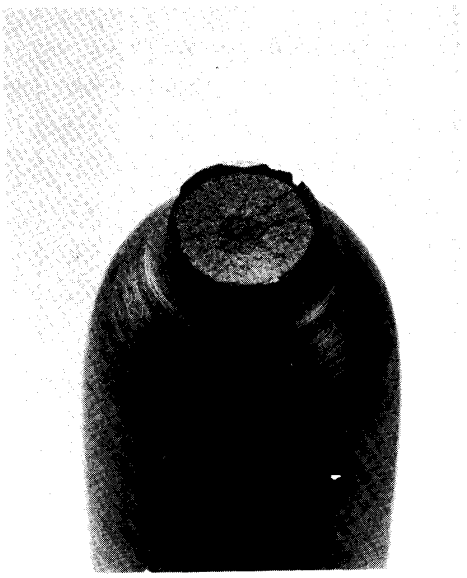

Fig.6 Light fractograph of S45C: fracture surface of Bridgman-type specimen. It shows typical bimodal fracture.

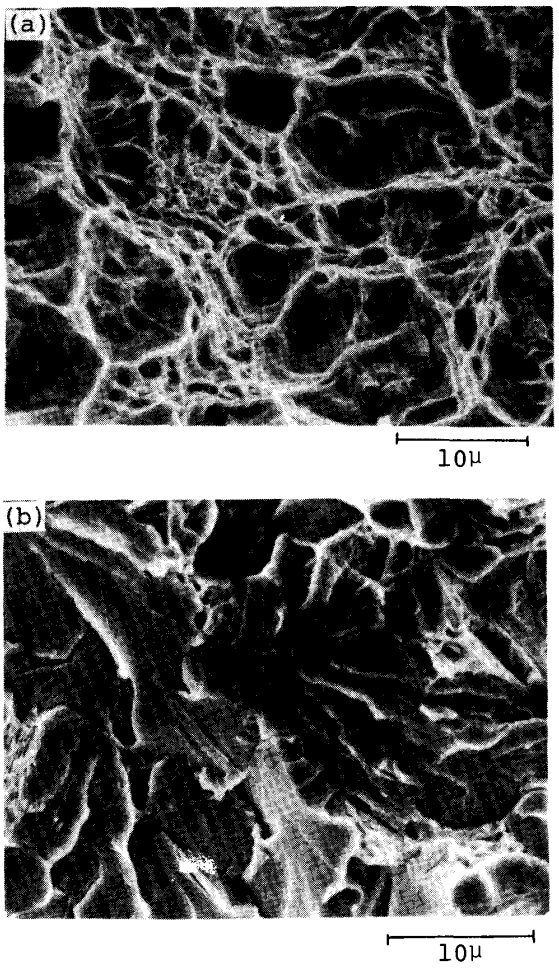

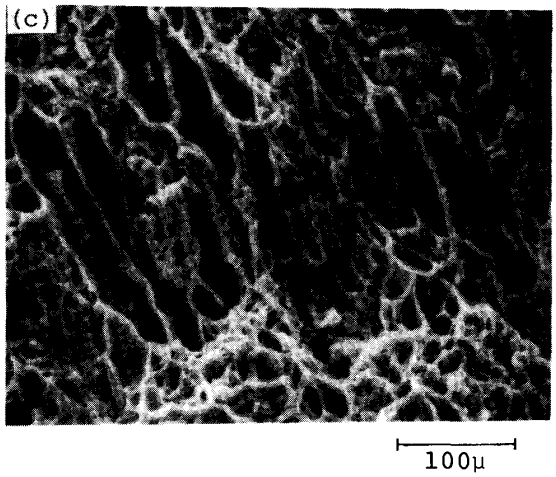

Fig.7 SEM fractograph of S45C. (a): dimple fracture mode in the central, fibrous zone in Fig.6 , (b): cleavage fracture mode in the outer zone in Fig.6, (c): shear mode dimple fracture in the circumferential zone in Fig.6 .

II. 2. 2. The failure map for S 25 C (Fig. 8)

S 25 C is a steel to roughly 0.25 wt.% carbon in iron (Table 2).

Table 2 Chemical composition of S25C (wt%)

C	Si	Mn	P	S	Cu	Ni	Cr
0.24	0.21	0.42	0.016	0.019	0.04	0.01	0.02

Figure8 shows that the same fields appear on its map as on that for S 45 C, but they are displaced to higher hydrostatic tensile stress and lower temperatures. The field of ductile fracture under room temperature is wide and the field of overall cleavage appears at -75° C and 60 kg/mm^2. Under conditions of low triaxial stress, the alloy displays high ductility but shows less strain to fracture in high triaxial stress. The fracture strain of the alloy is much highly dependent on the state of the stress than in the S45C.

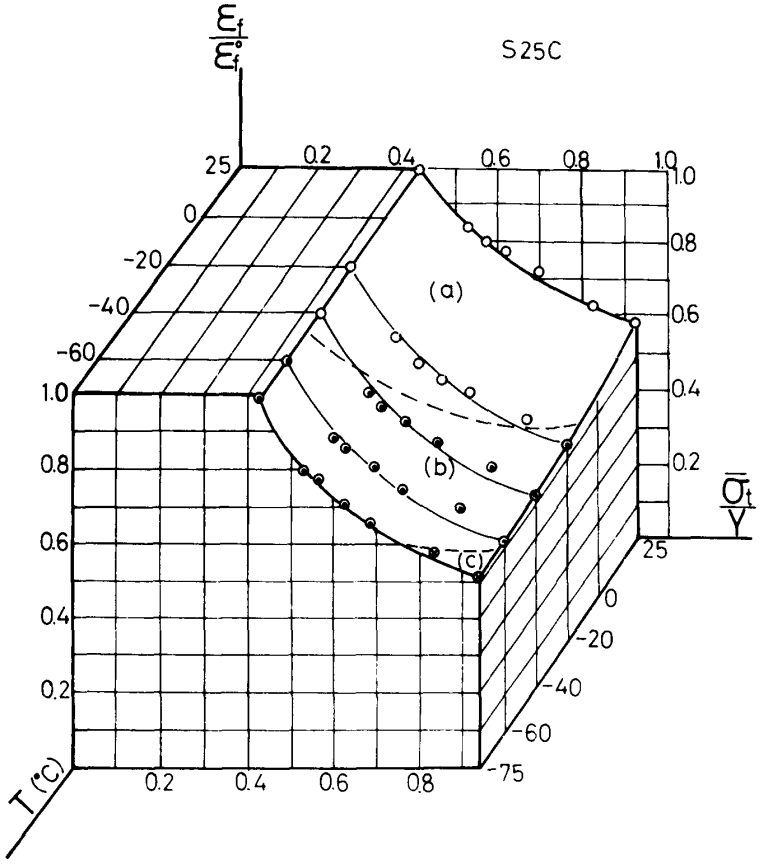

Fig.8 Failure map of S25C. (cross-head speed: 0.5 mm/min.)

II. 2. 3. The failure map for S M 50 (Fig. 9)

S M 50 is a low carbon steel which involved Silicon and Manganese and used extensively as structural material. (Table 3.)

Table 3 Chemical composition of SM 50

(wt%)

C	Si	Mn	P	S	Ni	Cr	V
0.16	0.44	1.42	0.017	0.004	0.01	0.01	0.07

Figure 9 shows a failure map for SM 50. The alloy fails by ductile fracture at room temperature and at low negative pressure, but the strain to fracture decreases abruptly as the value of negative pressure increases and as the temperature decreases, and the fracture mode changes abruptly from ductile to cleavage. As the temperature is decreased, it fails macroscopically by radial fracuture as shown in figure 10.

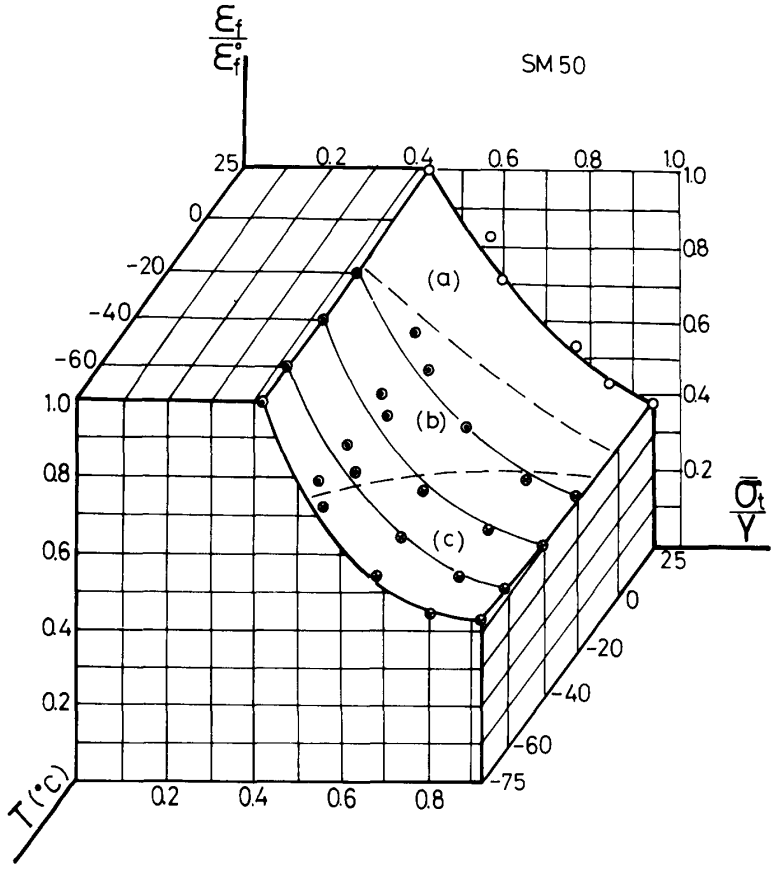

Fig.9 Failure map of SM50.

(cross-head speed : 0.5 $^{mm}/_{min.}$)

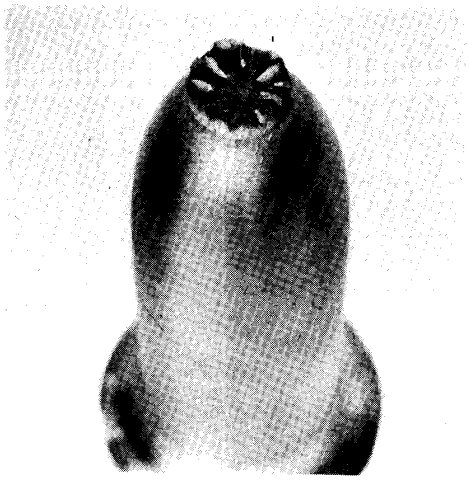

Fig.10 Light fractograph of SM50: fracture surface of Bridgman-type specimen. It shows typical radial fracture.

II. 2. 4. The failure map for high-purity Fe-30Cr-2Mo alloy (Fig. 11)

Fe-30Cr-2Mo alloy is one of the high-purity ferritic stainless steel produced by vacuum induction melting with relatively pure raw materials. The alloy has superior resistance to stress corrosion cracking and to pitting and crevice corrosion[16]. Important problems still to be solved are the toughness and the as-welded ductility and formability of thicker sheet. The chemical composition is given in Table 4.

Table 4 Chemical composition of Fe-30Cr-2Mo alloy

(wt%)

C	Si	Mn	P	S	Ni	Cr	Mo	Al	O	N	Nb
0.002	0.14	0.05	0.02	0.0]	0.17	30.3	1.9	1.1	0.002	0.006	0.1

The alloy needs a high annealing temperature with an attendant coarse-grained structure in conventional process.

Figure 11 shows a failure map for the alloy with coarse-grained structure. As seen in this figure, the higher the hydrostatic tensile stress and the lower the temperature, the lower the fracture strain. The influence of the hydrostatic tension on the fracture behaviour of the alloy is higher than that of carbon steels. While the fracture strain is very large in low triaxiality, it decreases abruptly as the value of hydrostatic tensile component increases. Boundary between ductile and bimodal exists in vicinity of room temperature.
The results suggest that special attention should be paid to the

conditions of deformation processing for this alloy with the coarse-grained structure and the conditions of practical use of the thick plate. Producing a fine-grained is a most effective means of preventing the occurrence of embrittlement, as shown as in another presentation[17)]

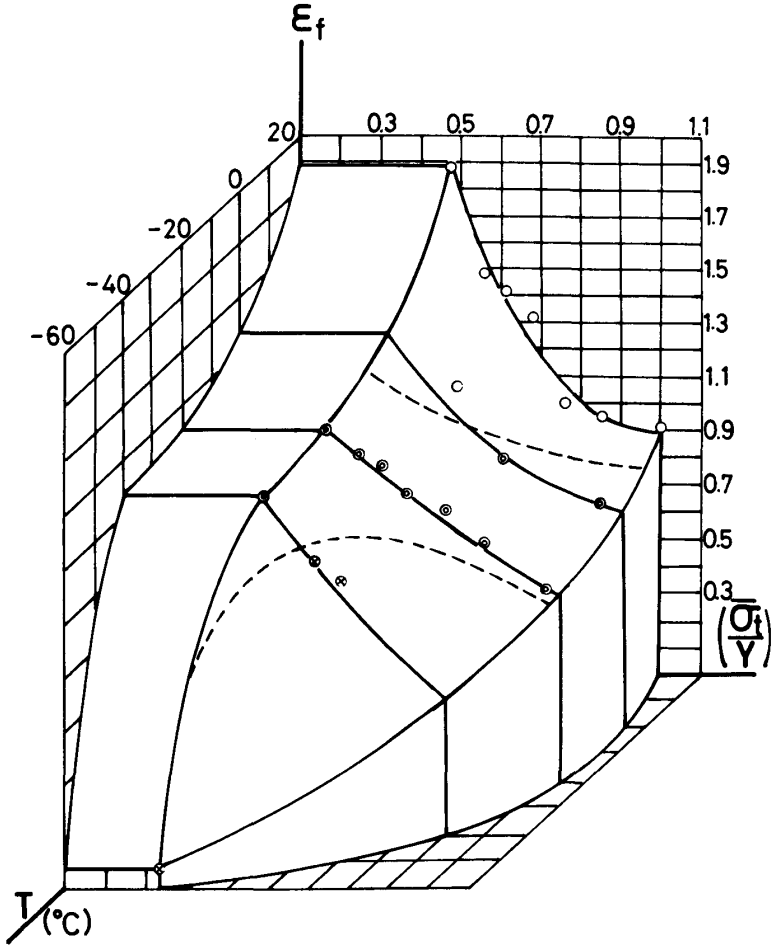

Fig.11 Failure map of high-purity Fe-30Cr-2Mo alloy
(cross-head speed : 0.5 $^{mm}/_{min.}$)

II. 3. Commercial structural nonferreous alloys

II. 3. 1. The failure map for Ti-6Al-4V alloy (Fig. 12)

Although Ti-6Al-4V alloy is a fairly well-investigated titanium alloy, there is a need for more characterization of the dependence of mechanical properties on pressure, temperature and microstructure. Of engineering alloys, those having the close packed hexagonal crystal structure are the most prone to texture induced anisotropy of physical and mechanical properties. Chemical composition and thermal and mechanical history of material used in this investigation are shown in Table 5 and 6.

Table 5 Chemical composition of Ti-6Al-4V alloy (wt%)

Al	V	Fe	N	O	H	C	Si
6.18	4.30	0.20	0.002	0.145	0.003	0.014	0.021

Table 6 Thermal and mechanical history of Ti-6Al-4V alloy

	forging		forging		
ingot	⟶	billet	⟶	round bar	⟶ annealing
	1100°C	(165×460×L)	850°C	(32φ)	700°C × 2hr A. C.

Tensile test specimens in the longitudinal direction were used. Microstructure of the specimen consisted of ~90 pct cph and ~10 pct bcc phase and texture was an alpha deformation.

Figure 12 shows a failure map for the Ti-6Al-4V alloy. As seen in the figure, the higher the hydrostatic tension, the lower the fracture strain, and the fracture strain decreases slightly as the temperature lowers. Fracture surfaces of all specimens revealed the ductile mode and any transition from ductile to cleavage was not found. For this point of view, it may be said that the alloy has a good ductility under the conditions of high hydrostatic tensile stress state and at low temperature.

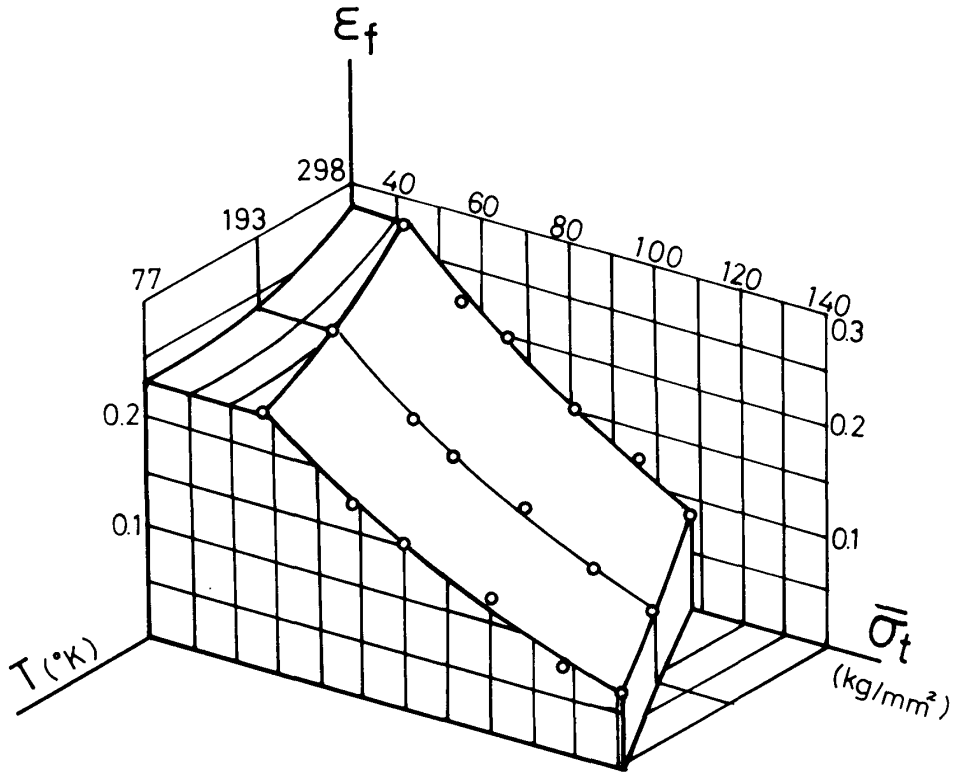

Fig.12 Failure map of Ti-6Al-4V alloy, ε_f: fracture strain, σ_t: mean maximum hydrostatic tensile stress, T: temperature. (cross-head speed : 0.5 mm/min.)

II. 3. 2. The failure map for 7075 aluminium alloy (Fig. 13)

7075 aluminium alloy is a high strength precipitation-hardened alloy, used in the wrought state by the aerospace industry. The alloy is worked, often by rolling; solution heat treated; and aged. During ageing, GP zones form first and are then replaced by η-phase. Because it is used in the wrought state, 7075 is anisotropic. We have selected data for specimens cut along the rolling direction. Table 7 shows chemical composition and thermal and mechanical history of the specimen.

Table 7 Chemical composition and thermal and mechanical history of 7075 aluminum alloy (wt%)

Si	Fe	Cu	Mn	Mg	Cr	Zn	Ti
0.07	0.21	1.6	0.01	2.6	0.19	5.6	0.01

ingot → homogenizing → hot rolling (thickness: 300→50mm)
460°C×24hr 400~440°C

Figure 13 shows a failure map for a 7075-T6 aluminium alloy. As seen in the figure, the higher the hydrostatic stress and the lower the temperature, the smaller the fracture strain. Under the room temperature the alloy fails by intergranular fracture.

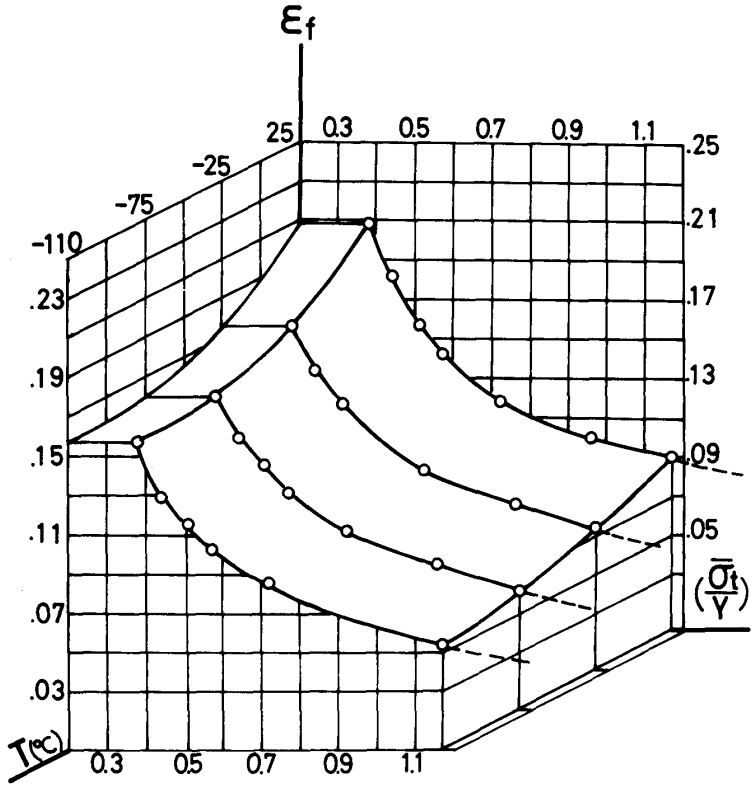

Fig.13 Failure map of 7075 aluminum alloy. Open circle in this figure shows intergranular fracture.
(cross-head speed : 0.5 $mm/_{min.}$)

In low triaxiality, the final fracture plane is at 45° to the tensile axis. The fact suggests shear-linkage of cracks.
Our observations are summarized in Fig.14 . Fig.14 (a) shows a type of intergranular fracture, starting from coarse inclusions on grain-boundary perpendicular to rolling direction. Fig.14 (b) shows the other type of intergranular fracture, separating grain-boundary parallel to the rolling direction. Fig.14 (c) shows a joining type of intergranular cracks in the state of high hydrostatic tension.

(a)

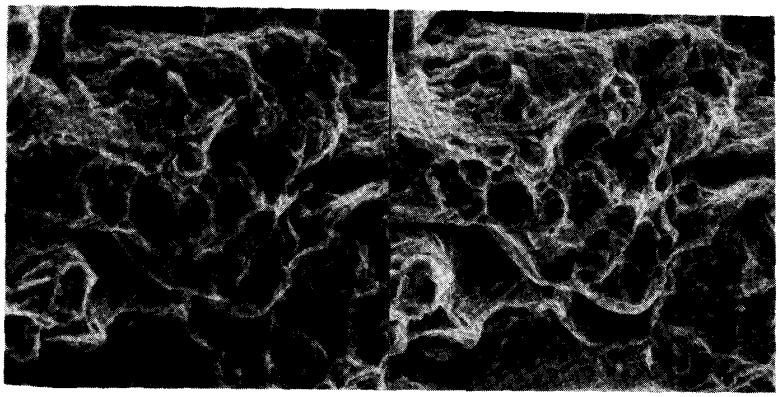

(b)

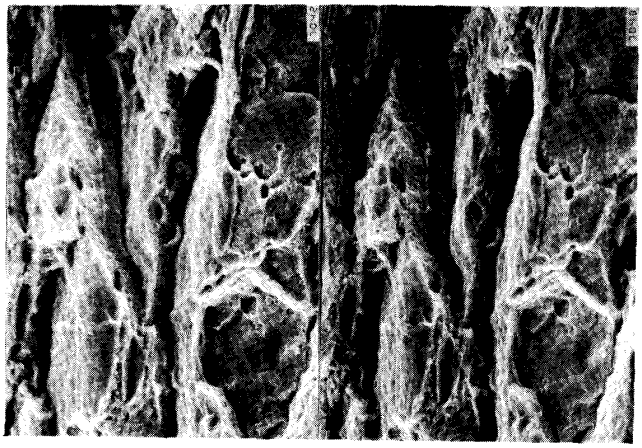

(c)

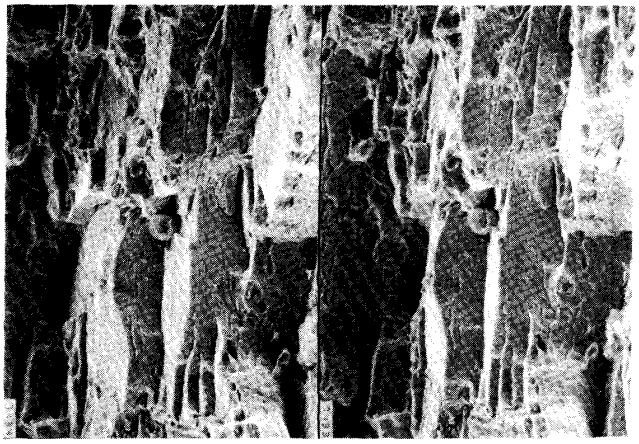

50μ

Fig.14 SEM stereo-fractograph of 7075 aluminum alloy, (a): a type of intergranular fracture, stating from coarse inclusions on grain-boundary perpendicular to rolling direction, (b): the other type of intergranular fracture, separating grain-boundaries parallel to rolling direction, (c): a joining type of intergranular cracks in the state of high hydrostatic tension.

One heat treatment, named T73 is sometimes applied on 7075 alloy for preventing stress corrosion cracking of the alloy. Figure 15 shows a comparison of fracture behaviour between 7075-T6 and 7075-T73 in cross-section of failure map at room temperature. Fracture strain is much higher in the 7075-T73 than in the 7075-T6 but it decreases more rapidly in the 7075-T73 than in the7075-T6 as the negative pressure increases. The 7075-T73 fails almost by transgranular ductile fracture.

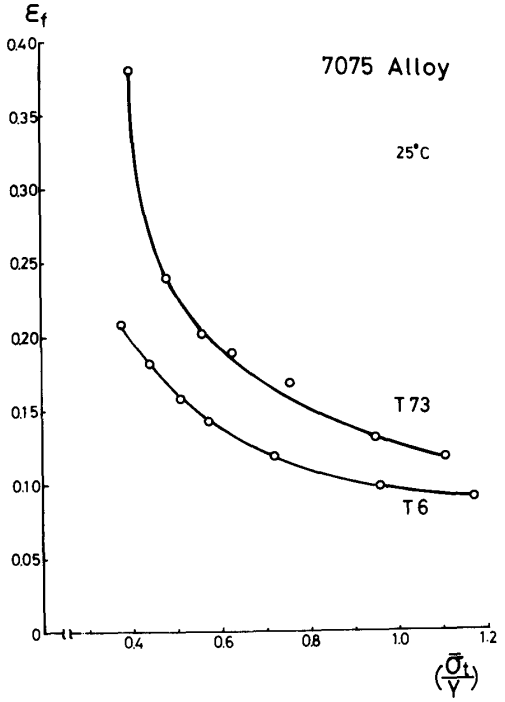

Fig.15 Comparison of fracture behaviour between 7075-T6 and 7075-T73 in cross-section of failure map at room temperature.
(cross-head speed : 0.5 mm/min.)

III. Conclusions

III. 1. The failure map as an overview of the fracture behaviour of materials

The observations of the fracture in hydrostatic tension of Bridgman-type specimens of various structural materials can be summarized as "failure map". A map for a given material shows the region of hydrostatic tensile stress, temperature and fracture strain over which a given mechanism of fracture is dominant. Most maps for structural steels show three principal fields under the room temperature, corresponding to ductile fracture, cleavage fracture and bimodal

fracture. Alloying, processing, structure etc. alter the extent and position of the fields. Failure map for a typical structural titanium alloy, Ti-6Al-4V, shows only one principal field of ductile fracture, nevertheless the "as-received" microstructure consisted of almost cph phase. Failure map for other typical structural nonferreous alloy, 7075-T6 alluminium alloy, shows also only one principal field of intergranular fracture under the room temperature. Origin of fracture is separation of grain boundaries parallel to the rolling direction in this case. Heat treatment alters characteristics of the field.

III. 2. Potential use and extension of the method

This presentation illustrates the basic formalism for the portrayal of the failure behaviour of materials. It should be emphasized that the work is at an early stage and is yet not to be regarded as a complete and useful methodology. However, the work indicates that the failure map may be used both to compare the behaviour of materials e.g. the competition between alloys to form a given component and on a more basic level to extend and compare the failure criteria applicable to bulk materials. For example, it is useful to illustrate the potential use of the failure maps by heat treatment material to promote a given failure mode and then examining the influence of the available strain paths on the resultant failure.

Finally, there is some hope that the approach might be extended to predict a way in which fracture toughness varies with stress and temperature. The fracture toughness of a material depends in a complicated way on the micromechanisms of plasticity and fracture occurring at the crack tip. There are some interesting problems, as follows; (1) Variation of fracture toughness of a material with hydrostatic pressure and relationship with tensile ductility[18], (2) Stable crack growth or transition of fracture mode in dynamic state, as shown in the case of structural steel[19], and (3) Simplified prediction of fracture toughness from tensile data[20].

Acknowledgements

The authors wish to thank Mr. Koyu Abe at Department of Precision Engineering, Tohoku University, for preparation of the specimens and Mr. Fumiyoshi Saito at Research Institute of Mineral Dressing and Matallurgy, Tohoku University, for tensile testing.

The structural steels used in this study were kindly provided by Nippon Steel Co., the Fe-30Cr-2Mo stainless steels by The Research Laboratory for Metals, Showa Denko Co., the Ti-6Al-4V alloys by Kobe Steel Co. and the 7075 aluminium alloys by Sumitomo Light Metals Co., respectively.

References

1) Rogers,H.C. in Proceedings. The Metallurgical Society of the American Institute of Mining, Metallurgical, and Petroleum Engineers, 1971, p.453.
2) Rice,J.R. and Tracey,D.M., Journal of the Mechanics and Physics of Solids, Vol.17, 1969, p.201.
3) Kula,E.B. and Argin,M., Deformation Processing, Ed. by V.Weiss, Syracuse University, 1977, p.245.
4) Ashby,M.F., Fracture 1977, Ed. D.M.R.Taplin, University of Waterloo Press, 1977.
5) Ashby,M.F., Gandhi,C. and Taplin D.M.R., Acta Metallurgica, Vol.27, 1979, p.699.
6) Embury,J.D. and LeRoy,G.H., Fracture 1977, Ed. D.M.R.Taplin, University of Waterloo Press, 1977, Vol.1, p.15.
7) Brown,L.M., The Mechanics and Physics of Fracture,Metal Society, London, 1976.
8) Francois,D., in Proceedings, Fourth International Conference on Fracture, Vol.1, 1977, p.805.
9) Aurich,D., Engang. Fract. Mech., Vol.7, 1975, 761.
10) Cridland,L. and Wood,W.G., The International Journal of Fracture Mechanics, Vol.4, 1968, p.277.
11) Bridgman,P.W., Studies in Large Plastic Flow and Fracture,McGraw-Hill Book Co., New York, 1952, p.9.
12) (a) Needleman,A., Journal of the Mechanics and Physics of Solids, Vol.20, 1972, p.111.
(b) Chen,W.H., International Journal of Solids and Structures. Vol.7, 1971, p.685.
(c) Norris,D.M. et al, Journal of the Mechanics and Physics of Solids. Vol.26, 1978, p.1.
13) Argon,A.S., Im,J., and Needleman,A., Metallurgical Transactions, Vol.6A, 1975, p.815.
14) Clausing,D.P., Journal of Materials, Vol.4, 1969, p.566.
15) Dondik,I.G., Problemy Prochnosti. No.8, 1970, p.54; also, Strength

of Materials, 1972, p.937.
16) Shimodaira,M., Saito,H., Morimura,T., and Hirano,T., presented at Japan Society of Corrosion Engineering, 12-14 May 1976.
17) Saito,S., Tokuno,H., Shimura,M., Tanaka,E., Kataura,Y., and Ototani,T., Toughness of Ferritic Stainless Steels, Ed. R.A.Lula, ASTM STP 706, 1980, p.77.
18) Auger,J.P., and Francois,D., International Journal of Fracture, Vol.13, 1977, p.431.
19) Crooker,T.W., Fracture Mechanics, ASTM STP 605, 1975, p.333.
20) Baskes,M.I., Enbineering Fracture Mechanics, Vol.7, 1975, p.249.